Experimental and numerical acoustic characterization of ultrasonically absorptive porous materials

Alexander Wagner* and Jan Martinez Schramm†
German Aerospace Center (DLR), Institute of Aerodynamics and Flow Technology, Göttingen, Germany

Christian Dittert‡
German Aerospace Center (DLR), Institute of Structures and Design, Stuttgart, Germany

Victor C. B. Sousa§, Danish Patel¶ and Carlo Scalo‖
School of Mechanical Engineering, Purdue University, West Lafayette, USA

The paper addresses the experimental and numerical acoustic characterization of ultrasonically absorptive porous materials with random microstructure such as carbon fiber reinforced carbon ceramic C/C or C/C-SiC. The present study builds upon previous efforts by the authors, improving and extending the established experimental method, complemented by a numerical analysis based on linear acoustics. The latter includes a blind-hole porosity approximation, only accounting for the larger cracks in the C/C with complex acoustic impedance given by the inverse Helmholtz Solver approach, and a highly parametrized homogeneous acoustic absorber model, accounting for the complete volumetric structure of the porous absorber albeit with lower fidelity. The experimental approach is complemented by high-speed Schlieren visualization and Mach-Zehnder Interferometer measurements to qualitatively and quantitatively assess the interaction between an ultrasonic wave packet and a porous surface. It is found that neglecting the smaller pores and only accounting for the surface porosity, as done in the blind-hole porosity approximation, leads to the underestimation of the acoustic energy absorption coefficient. Phase shifts were found to be experimentally assessable, but remain to be corroborated by a numerical analysis. The comparisons carried out in this paper will pave the way for accurate determination of impedance boundary conditions to be applied in direct numerical simulations of hypersonic transition delay over C/C. The main emphasis of the paper is to assess the potential and the limitations of the experimental methods and the comparison of the experimental results to the numerically obtained absorption characteristics.

I. Introduction

In flow fields with small free-stream disturbances, negligible surface roughness and predominantly two-dimensional hypersonic boundary layers second-mode instabilities are known to be the dominant mechanism leading to transition. Due to the acoustic nature of the instability ultrasonically absorptive coatings have the potential to damp the instabilities and thus delay laminar-turbulent transition [1]. Preceding studies in hypersonic wind tunnels indeed revealed that porous surfaces, such as metal sheets with cylindrical blind holes, felt metal and carbon fiber reinforced carbon ceramic (C/C) can be used to damp hypersonic boundary layer instabilities and thus passively control boundary layer transition.[2–9]

However, to achieve practical relevance the ultrasonically absorptive materials need to withstand the high shear stresses and heat loads present in hypersonic sustained flight. Such a material is for instance C/C-SiC which has been used successfully as TPS on hypersonic vehicles, [10, 11], and which can be manufactured with a comparable porosity and microstructure as found on C/C.[12] To assess the potential of such a material with respect to transition control the requirement arises to determine the ultrasonic absorption characteristic at the surface. For this purpose a test rig was set up at DLR Göttingen to measure the reflection coefficient at varying static pressures as reported in Wagner et al. [13].

*Research Scientist, Spacecraft Department, Alexander.Wagner@dlr.de
†Group Leader Aerothermodynamics, Spacecraft Department, Jan.Martinez@dlr.de
‡Research Scientist, Department of Space System Integration, Christian.Dittert@dlr.de
§Graduate Research Assistant, vsousa@purdue.edu.
¶Graduate Research Assistant, AIAA Student Member, patel472@purdue.edu
‖Assistant Professor, AIAA Member, scalo@purdue.edu

The improved setup uses ultrasonic sound transducers covering a frequency range of 125 kHz to 490 kHz and thus include a wide range of the frequency domain of interest with respect to the second mode instabilities.

On the numerical side, the inverse Helmholtz solver methodology [14, 15] is used to directly evaluate the broadband acoustic impedance associated with the C/C approximated as drilled-hole (or blind) porosity. The iHS methodology is hence only applied to a limited number of cracks in the C/C (the larger ones). Comparisons with experiments show that this simplification results in the underestimation of the overall absorption coefficient, especially at higher frequencies; it is therefore concluded that, especially in the latter case, even the smaller, more randomly distributed cavities contribute to the acoustic absorption. Results from the homogeneous absorber theory [16] are also included, which demonstrate a superior matching with the experiments, showing that the blind-hole porosity approximation (relying on surface porosity only) is insufficient to correctly account for the absorption capabilities of the C/C.

II. Method

A. Experimental Setup

1. Transducer Based Setup

Ultrasonic air-coupled PZT* sound transducers with specific resonance frequencies are arranged pairwise to transmit ultrasonic wave packets towards a material of interest and to record the wave packet after its reflection from the surface. Sound transducers with resonance frequencies of 125 kHz, 289 kHz, 300 kHz, 405 kHz and 490 kHz are used in the present study at an angle of incidence of 30° and a distance of 40 mm such that the transducer axes intersect at the sample surface. Figure 1 shows a schematic of the setup while table 1 provides the geometric parameters introduced in the figure. The angle of incidence was chosen based on experimental work performed by Fedorov et al. [17]. Further, it

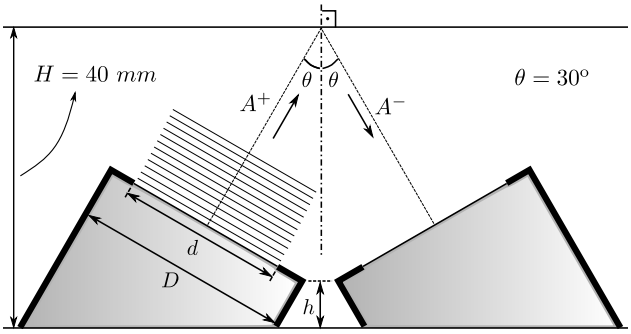

Fig. 1 Schematic of the experimental setup using ultrasonic sound transducers - transmitter on the left, receiver on the right (not to scale).

is justified by a numerical investigation conducted by Brès et al. [18] showing that in all cases relevant for ultrasonically absorptive coatings the angle of incidence of second mode waves is smaller than 26°. Further information on the experimental setup is provided in Wagner et al. [13].

2. Qualitative Schlieren Measurements

A high-speed Schlieren setup (in a z-type shaped arrangement) is used to visualize the generated sound waves as they propagate towards the test sample from which they are reflected. The optical setup is illuminated by a Cavitar Cavilux Smart laser system, which is operated with a pulse width of 20 ns. A Phantom v2012 camera is used with a resolution of 640px x 480px at a frame rate of 70 kHz to capture the development of the sound waves. No other light, other than that from the laser system, exposes the camera chip. This means that the laser pulse duration determines the exposure time, limiting motion blur to about 7 μm. Quantitative measurements beyond the Schlieren visualisation are planned using an interferometric method, which is introduced below.

*Plumb-Zirconate-Titanate piezoelectric ceramic

f $[kHz]$	d $[mm]$	D $[mm]$	h $[mm]$
125	19	30	1
223	11	17	0
289	7	17	0.7
300	7	17	1
405	9	17	0
490	8	17	0

Table 1 Geometric parameters of the transducer/receiver pairs.

3. Quantitative Mach-Zehnder-Interferometer Measurements

In order to obtain complementary measurements to the one dimensional temporally resolved recording with the sound transducers an optical setup based on a Mach-Zehnder-Interferometer (MZI) built by Carl Zeiss in 1926 was implemented. The sound waves created by the PZT transducers are visualized and quantitatively evaluated based on interferometric measurements of the wave distribution. The experimental setup and measurements obtained with it will be described and the possibilities and challenges of this measurement technique when applied to the current experiments are discussed. A high speed camera in combination with the MZI is used to image the sound waves as they propagate towards the test sample. A schematic of the optical setup is given in figure 2. A green diode-pumped solide-state cw-laser (5320nm ,230mW) is used to illuminate the system. A non-resonant mode cleaning setup consisting of a focusing lens L1 = 20 mm and a pinhole P having a diameter of 20 μm is used to optimize and shape the beam profile of the laser. A second lens L3 = 40 mm expands the laser beam onto the forming lens L3 = 500 mm after which is becomes parallel. The parallel laser beam is then fed into the MZI. Here the laser beam is split into a reference path and the object path by means of two half mirrors (HM) and reflecting it with two full mirrors (FM). Both beams are collimated through the lens L3 = 500 mm and focused on the chip of the high speed camera, where they interfere. The high speed camera capturing the images is a Phantom v2012, equipped with the FAST option, and is used at a resolution of 640x384px^2 and frame rate of 77kHz. The exposure time is set to the lowest possible value, which is 0.285 μs for the Phantom v2012. The time shift between the recording of consecutive images is 12.98 μs.

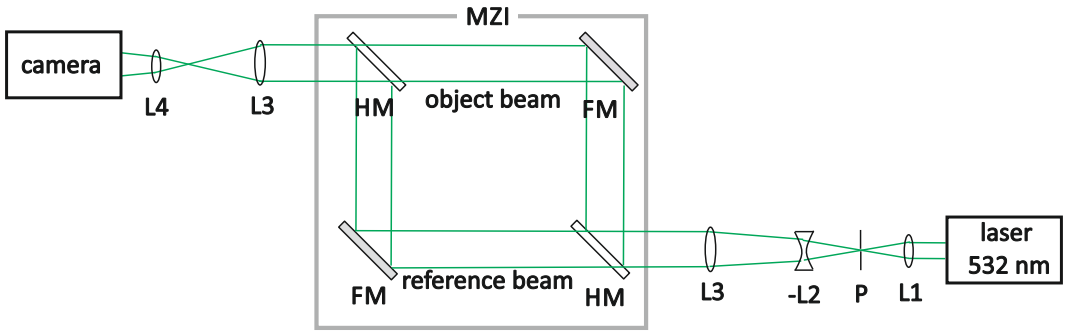

Fig. 2 Schematic of the optical setup using a Mach-Zehnder-Interferometer (MZI). Non resonant mode cleaner (L1, P, -L2), main lenses (L3,L4), HM: half mirror and FM: full mirror are parts of the MZI.

The optical resolution of the system is determined with a 1951 USAF resolution test chart conforming to MIL-STD-150A standard (set by US Air Force in 1951) to be 198.43 μm (see figure 3b)). Transforming the frequency of f = 125 kHz used for the sound transducers at the current tests, we observe a wavelength of 2.74 mm. Therefore, we are able to resolve one wavelength with approximately 14 data points or pixels on the chip. A better resolution is not feasible, because of the limit of minimal exposure time of the camera, which introduces a motion blur of approximately 87 μm. Quantitative measurements of the pressure waves observed in the object beam of the MZI are based on the interference pattern formed by the superposition of light waves which originate from the coherent source of the laser but traverse different paths (object beam and reference beam, see figure 2). The fringe pattern indicates the local phase shifts arising from the difference in the optical paths traversed by the interfering beams.

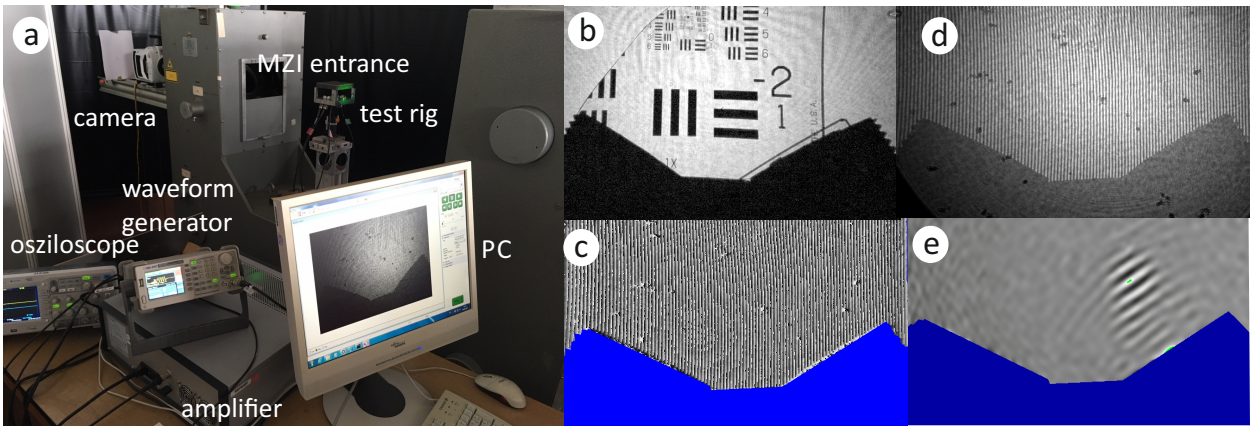

Fig. 3 A photograph of the experimental setup is shown in a), a camera image of object beam with the optical resolution target is given in b). A typical interference pattern between the object and the reference beam without any phase change in the object beam is shown in d). The reconstructed interference pattern with a 2D-FFT is given in c) and the evaluated phase shift distribution of a wave packet in e).

The resulting interference pattern without any introduced phase change in the object beam can be controlled by adequate adjustment of the half and full mirrors of the MZI. In order to use a two-dimensional Fast-Fourier-Transformation (2D-FFT) to evaluate the phase distribution from the interferograms, we create spatial carrier fringes as shown in figure 3d). The procedure is standard and well documented in the literature ([19–23]), therefore only a short summary is provided. The spatial intensity distribution of the fringe pattern, determined by the object beams phase shift Φ and the spatial carrier phase, can be written as

$$I(\vec{r}) = I_0(\vec{r}) + m(\vec{r})\cos(2\pi\nu_0(\vec{r})\vec{r} + \Phi(\vec{r})),$$

where I_0 and m are the background and contrast functions, ν_0 is the carrier frequency vector with components for the x- and y-direction and $\Phi(x, y)$ is the required phase function. If the largest gradient from the object phase is less than the spatial carrier phase and ν_0 is less than half of the sampling frequency Nyquist condition), then the phase distribution can be determined in both magnitude and sign. The above equation can be transformed into

$$I(\vec{r}) = I_0(\vec{r}) + c(\vec{r})e^{(2\pi i\nu_0\vec{r})} + c^*(\vec{r})e^{(-2\pi i\nu_0\vec{r})}$$

where

$$c(\vec{r}) = \frac{1}{2}m(\vec{r})e^{i\Phi}.$$

The superscript (*) denotes the complex conjugate. The Fourier transform of I(x,y) yields

$$\widehat{I}(\vec{r}) = \widehat{I_0}(\nu) + \widehat{c}(\nu - \nu_0) + \widehat{c}^*(-\nu - \nu_0).$$

This clearly reveals the purpose of generating the fringe carrier system: Disturbing changes in background intensity I_0 are of lower frequencies. By applying a comparable high carrier frequency ν_0, the information of the fringe system is separated from the disturbing low frequencies in the Fourier domain, shifting it to the vicinity of ν_0. The determination of the phase distribution $\Phi(r)$ is straight forward. First the domain $c(\nu - \nu_0)$ of the interferogram around the carrier frequency is determined via the FFT, then all frequencies outside this domain are set to zero. Then the domain centered around ν_0 is transferred towards the origin (zero-frequency), which removes the carrier. This resulting frequency field is the inverse Fourier transformed yielding $c(r)$. Finally the phase modulo 2π (see figure 3e)) is calculated by

$$\Phi(\vec{r}) = \arctan\left(\frac{Im(c(\vec{r}))}{Re(c(\vec{r}))}\right).$$

B. Numerical Setup

The methodology used to determine the complex acoustic impedance of the blind-hole porosity approximation of the C/C is the inverse Helmholtz Solver (iHS) [14, 15].

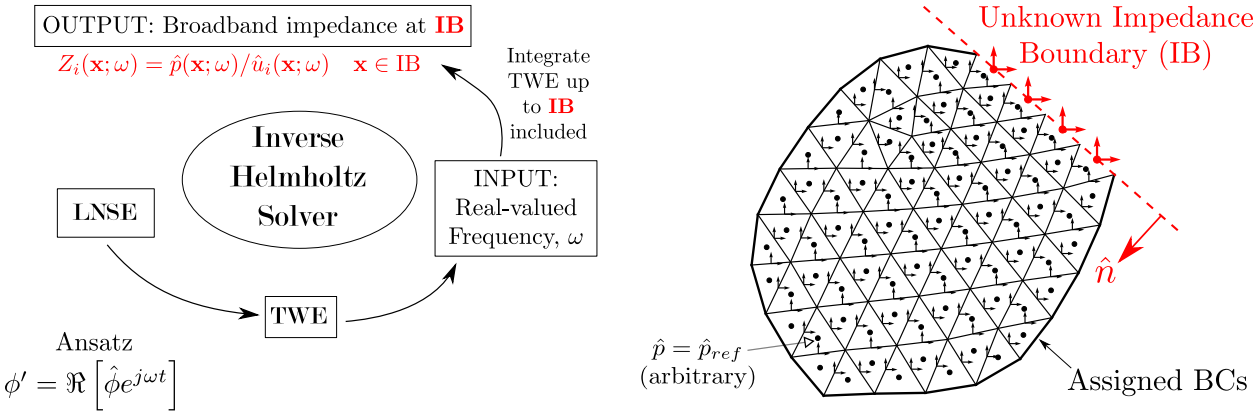

Fig. 4 Inverse Helmholtz solver procedure used to calculate the impedance of cavities typical of blind-hole porous surfaces.

This code reconstructs, at a given frequency, the complex acoustic waveform in the cavity up to the open surface or unknown impedance boundary (IB), hereby providing the complete spatial distribution of impedance as a result of the calculation. Multiple instances of the iHS can be executed in parallel for different frequencies, allowing for a rapid determination of the full broadband impedance at every point of the IB.

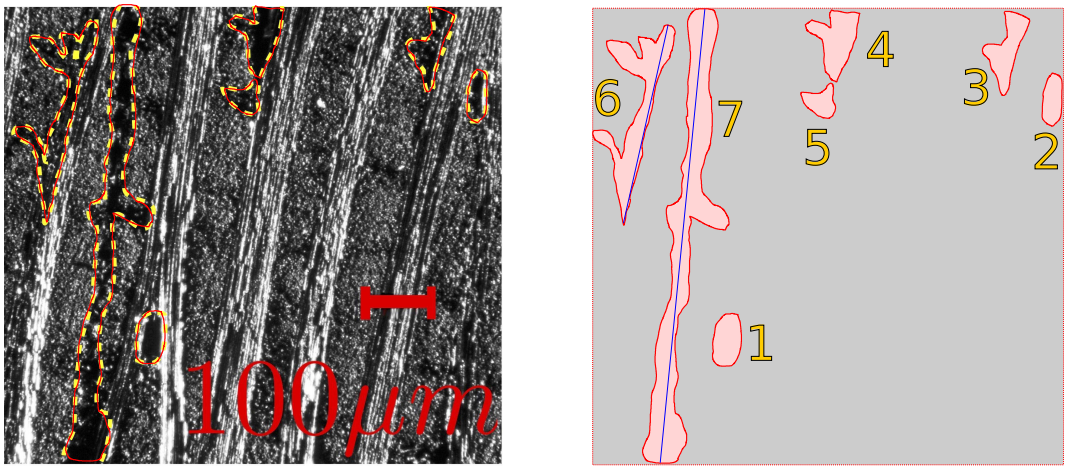

Fig. 5 Inverse Helmholtz solver procedure used to calculate the impedance of cavities typical of blind-hole porous surfaces.

From a high definition image of the C/C block (figure 5), large cavity edges are detected and meshed to be fed as input to the iHS. The impedance for various cavities are then evaluated by the solver and combined together–noting that the admittance of the surrounding hard surface is zero–to yield the effective, surface averaged impedance of the block.

III. Results

A. Experimental Results

1. Qualitative Schlieren Visualization

The high speed schlieren setup described in section A was used to visualize the ultrasonic waves generated by the sound transducers in the above introduced setup. Although the signal to noise ration is low, waves at 125 kHz, 300 kHz and 490 kHz were successfully visualized at ambient pressures as shown in figure 6. The schlieren images resemble the schematic in figure 1 in which the ultrasonic wave packets are generated by the transducer on the left. Subsequently the waves propagate along the transducer axis towards the investigates sample surface at the top of the image and are reflected back towards the receiver. The schlieren visualizations provide vital qualitative information, such as the dispersion angle of the sound waves, the point of interaction at the sample and the receiver and the wave dimensions. These information are required to numerically reconstruct the experiment. Unfortunately, the signal to noise ratio is too low to allow a quantitative evaluation of the wave amplitudes for instance.

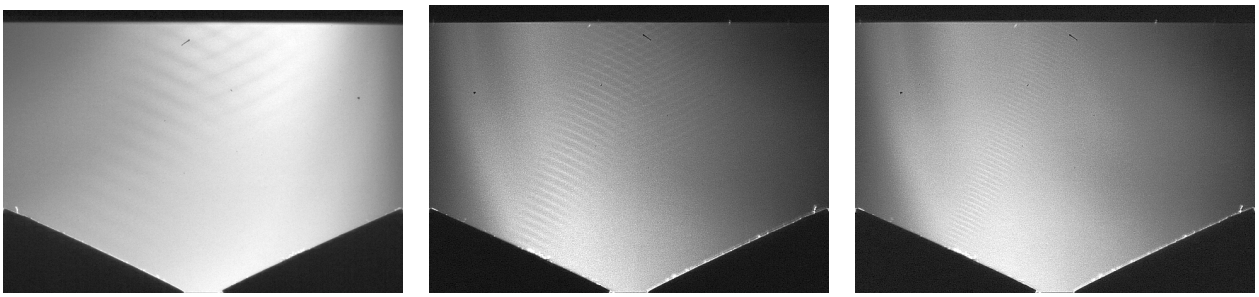

(a) f = 125 kHz (b) f = 300 kHz (c) f = 490 kHz

Fig. 6 Schlieren visualizations of ultrasonic waves at 125 kHz, 300 kHz and 490 kHz at ambient pressure.

2. Absorption Coefficient Measurements by means of Sound Transducers

Figure 7 provides representative results of the measured absorption coefficient of a C/C sample ([24]) using an optimized experimental setup, compared to the setup introduced in Wagner et al. [13]. The absorption coefficient is provided as a function of pressure in a frequency range of 125 kHz to 490 kHz. The optimized setup now allows conducting tests at pressures as low as approximately 2500 Pa. Note that the lowest pressure at which absorption measurements can be conducted depends on the sound wave frequency. The now accessible low pressure range is of particular interest regarding possible applications o ultrasonically absorptive materials for transition control on hypersonic vehicles.

Figure 7 shows some important trends which were repeatably observed on various investigated porous materials:

- a dependency on ambient pressure: the absorption coefficient decreases with decreasing ambient pressure, in particular in the low pressure range,
- a dependency on the frequency: the absorption coefficient increases with increasing frequency and
- with regard to the measurement technique: increasing uncertainties with decreasing ambient pressure.

The provided measurement errors are derived by evaluating a series of independent measurements with an acoustically hard surface. Since the reflection coefficient of that test case is known to be unity a mean, ambient pressure dependent, measurement error could be determined as indicated in figure 7. Note that this error does not account for locally changing surface properties.

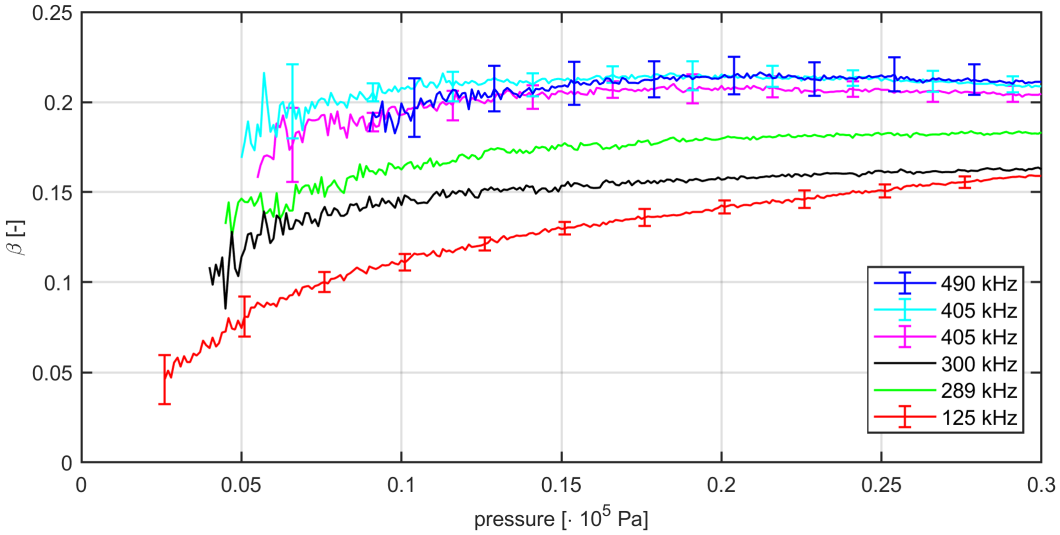

Fig. 7 Absorption coefficient experimentally obtain on a C/C sample using sound transducers at different frequencies.

3. Sound Transducer Phase Shift Measurements

In the course of the experimental study the question was raised whether the setup could be used to measure the expected and numerically predicted phase shift resulting from the reflection of the sound wave at a porous wall. This would allow to fully acoustically characterize the sample of interest by determining the reflection coefficient and the phase shift and thus the real and imaginary part of the surface impedance. To address this issue the setup described in section A was used in combination with an acoustically hard surface positioned with a sub-wavelength offset from the reference position. The offset was realized using metal sheets of 0.3 mm thickness. Figure 8 shows the time resolved

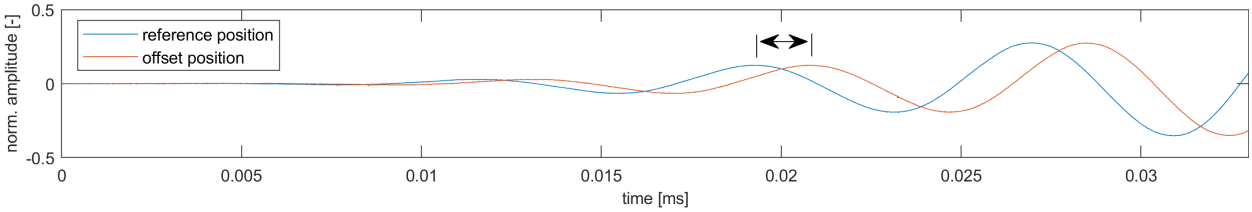

(a) f = 125 kHz

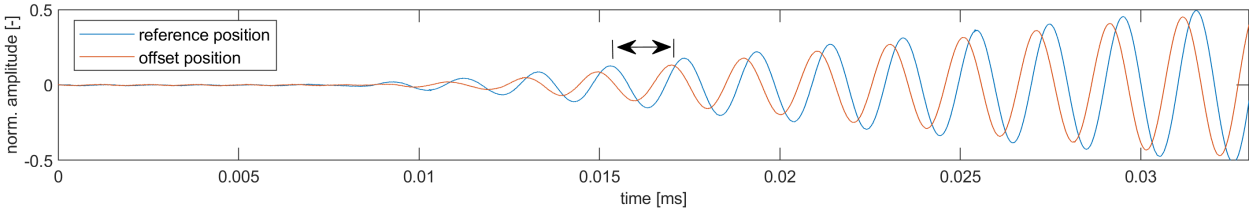

(b) f = 490 kHz

Fig. 8 Time resolved reflected sound waves with 125 kHz and 490 kHz. The indicated phase shift results from a position offset of the reference sample.

normalized pressure measurements at the receiver after the sound wave reflection at the wall. Tests were conducted using two different frequencies; 125 kHz shown in figure 8a and 490 kHz shown in figure 8b. Both figures depict the first periods of the wave packets after reflection at an acoustically hard surface at the reference position (shown in blue) and the surface positioned with an offset (shown in red). It can be seen that the latter shows a phase shift compared to the reference case. This phase shift corresponds to the change of the path length experienced by the acoustic wave due

to the altered position of the reflection surface. An evaluation of the phase shift of multiple wave packets allows to determine the distance of the reflection surface is shown in figure 9. The speed of sound in the nitrogen test atmosphere

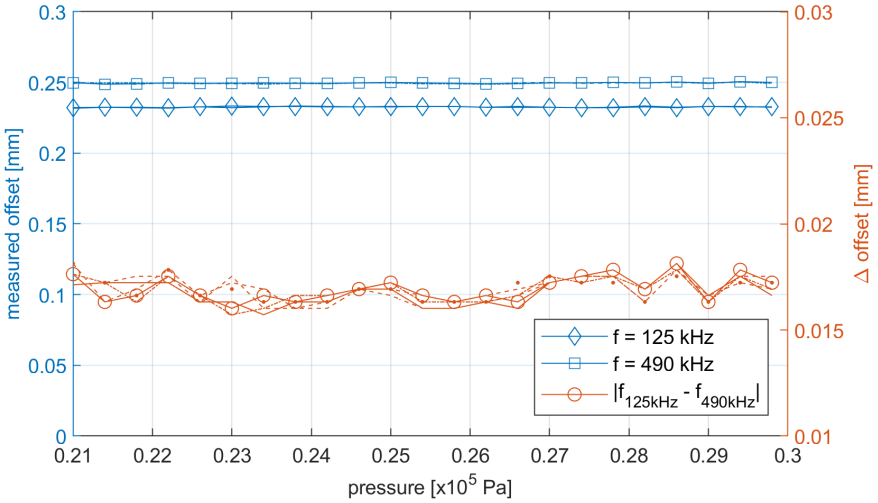

Fig. 9 Measured offset from the reference position (left) and approximate resolution limit (right).

was estimated with 349 m/s assuming a test gas temperature of 293 K. However, the gas temperature was not monitored during the tests adding to the uncertainties of the measurements. Note that the precise value of the offset is also subject to a number of uncertainties linked to the installation of the metal sheets. However, the distance between the reflection surface and the transducer pairs is expected to be identical. Thus, a comparative measurement between the 125 kHz and the 490 kHz transducers provides a first estimate of the achievable precision. Figure 9 shows that the independent measurements differ by approximately 0.017 mm which corresponds to 2.2 degree and 8.6 degree of the 125 kHz and the 490 kHz sound wave. These values provide an estimate of the smallest resolvable phase shift. Further improvements of the setup are necessary to reduce the positioning uncertainty of the investigated sample before assessing possible phase shifts due to the interaction of the sound wave with a porous surface.

4. Preliminary Results of the Wave Propagation determined by Interferometric Measurements

A first result of the observed waves is given in figure 10. The test rig was installed without a reflective surface in the object beam of the MZI. A wave packet with a frequency of f = 125 kHz was generated with 4 periods. The image sequences given in 10 show the temporal and spatial two dimensional evolution of the wave packet generated by the sound transducers. The propagation of the wave packet can clearly be observed and the spatial broadening perpendicular to the direction of motion can be determined. The first recording at t = 12.98 μs shows the appearance of two waves (1/f = 1/125 kHz = 6 μs), one image later, the complete packet (4 periods) is visible. As the packet travels along the propagation direction, it can be observed that additional weak waves are emitted behind the wave packet. This is due to the decay of the transducer.

In figure 11 the phase data along the symmetry line of the propagation direction is shown for different instants in time. The data is extracted from the images shown in 10. For reference purposes, the data at t = 0 μs is added to every graph as a red line. The propagation and damping of the wave packet over time can be observed until it leaves the field of view. We note at this point, that the signal to noise ratio is approximately 5 in average over all data obtained. To improve this ratio, the measurements can only be performed in a different gas than air, which would yield stronger signals. To investigate how far the analysis of the data can be driven, a set of 10 consecutive recordings of a continuous generated waves of f = 125 kHz are spatially averaged. We compare the averaged data of the incoming and the reflected waves in figure 12 for a solid wall and a porous wall.

The data in figure 12a) compares the recorded waves approaching the walls (incoming waves). The repeatability for the different experiments is very good. The comparison for the waves which return from the walls after reflection (reflected waves) in figure 12b) reveals the differences of both waves after the reflection at the solid and the porous wall. The amplitude is obviously lower, but a distinct phase shift cannot be observed.

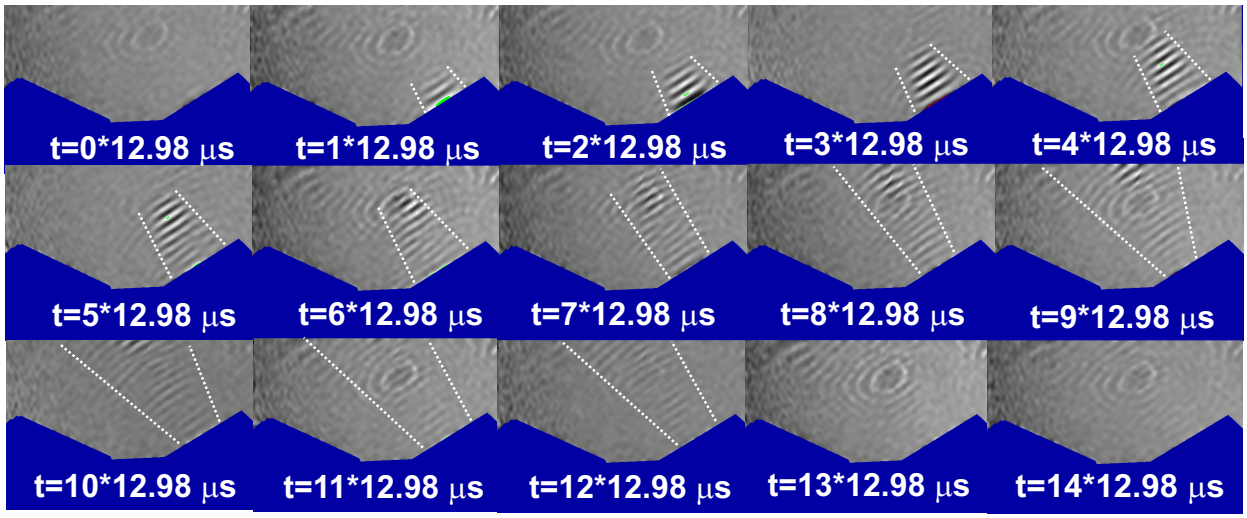

Fig. 10 Temporal and spatial evolution of the sound waves. The test rig is used without a reflective wall.

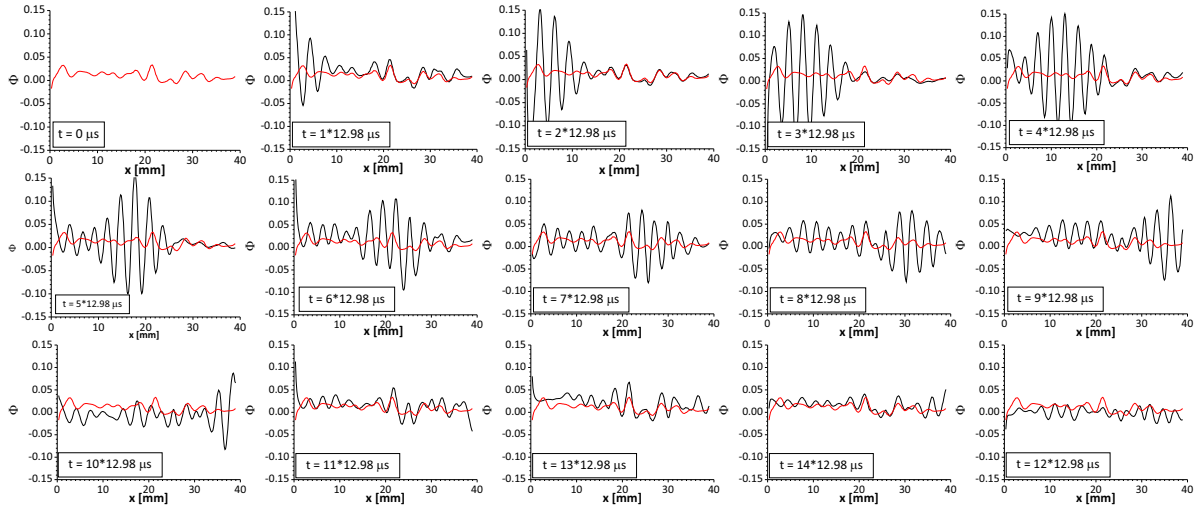

Fig. 11 Temporal evolution of the sound waves along the symmetry line of the propagation direction. The red curve is the reference recording at t = 0 μs. The test rig is installed without a reflective plate.

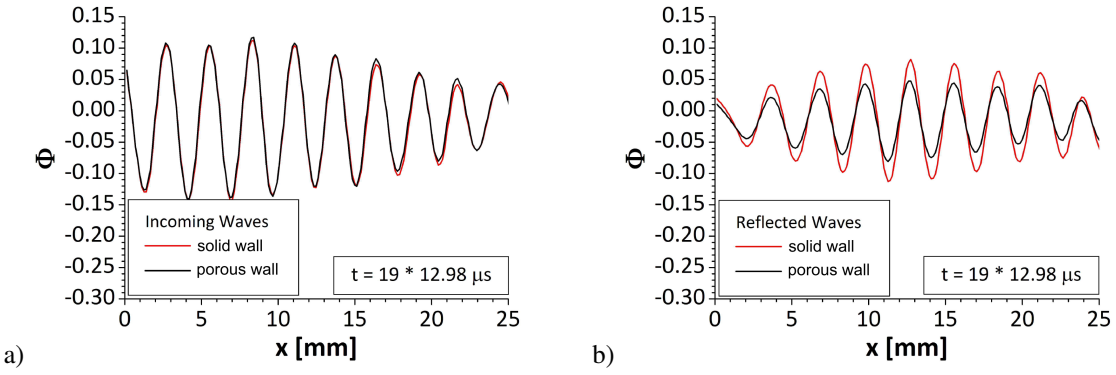

Fig. 12 Wave distribution of incoming waves and reflect waves for different surfaces.

B. Numerical Results

The iHS was used to evaluate the effective surface-averaged specific acoustic impedance of the C/C surface approximated as blind-hole porosity and only composed of the larger pores, as shown in figure 5. This yields a surface porosity of 0.078 which is extruded in the depth, hence yielding the same assumed volumetric porosity. A broad range of conditions is covered, bracketing experimental conditions.

Comparison were then made between numerical and experimental results as well as with the homogeneous absorber theory, a theoretical model that calculates the acoustic impedance of a homogeneous porous absorber accounting for the whole volumetric distribution of the pores. A value of volumetric porosity equal to 0.15 is used in this approach, which is almost twice the porosity used in the blind-hole approximation of the C/C.

The variable of choice for these comparisons is the acoustic absorption coefficient, β, which is a quantitative estimate of the amount of acoustic energy absorbed at the C/C surface due to the presence of microporous cracks. The absorption coefficient relates to the acoustic impedance via,

$$\beta(\omega) = 1 - \left| \frac{1 - Z_*(\omega)}{1 + Z_*(\omega)} \right|^2, \tag{1}$$

where $Z_*(\omega)$ is the broadband surface averaged specific acoustic impedance of the C/C absorber.

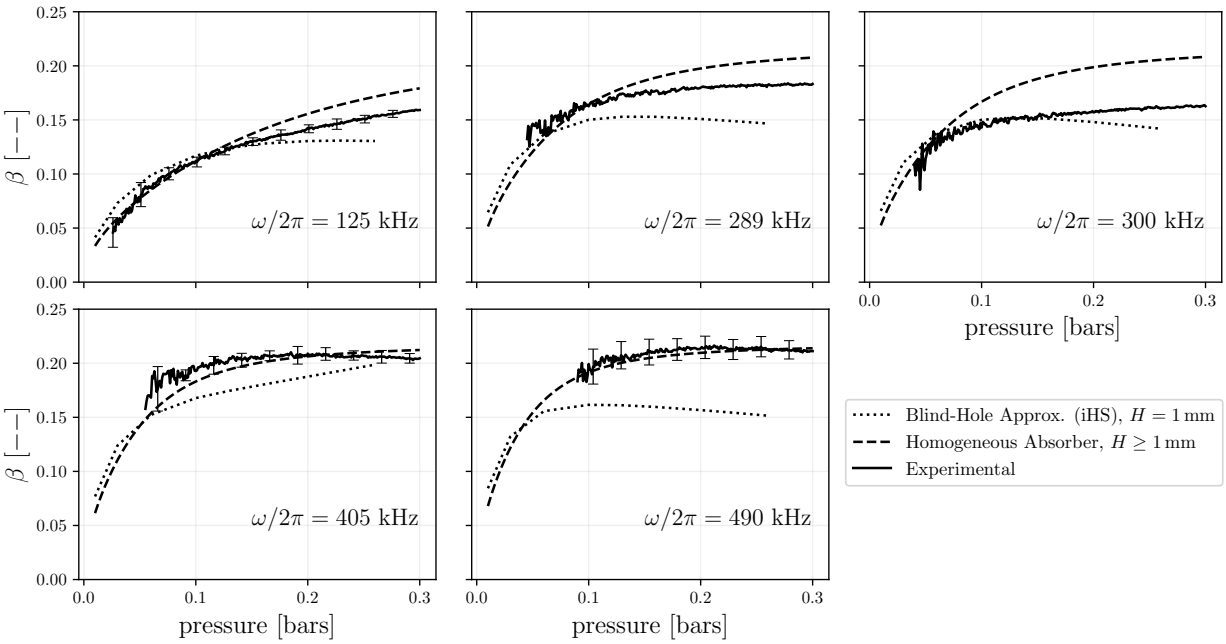

Fig. 13 Comparisons in the variation of numerically, theoretically, and experimentally evaluated absorption coefficients, β, with ambient pressure.

Homogeneous Absorber Theory

The homogeneous absorber theory [16] defines the impedance of a volumetric porous absorber subject to wave incidence at the angle θ_i as,

$$Z_{\text{abs}} = Z_\infty \frac{1 + e^{-j2k_a H}}{1 - e^{-j2k_a H}} \cos(\theta_i) \tag{2}$$

with,

$$k_a = k\sqrt{\kappa}\sqrt{1 - j\frac{\omega_k}{\omega}}, \quad Z_\infty = Z_0 \frac{\sqrt{\kappa}}{\phi}\sqrt{1 - j\frac{\omega_k}{\omega}}, \text{ and } \omega_k = \frac{\Xi\phi}{\rho_0 \kappa}$$

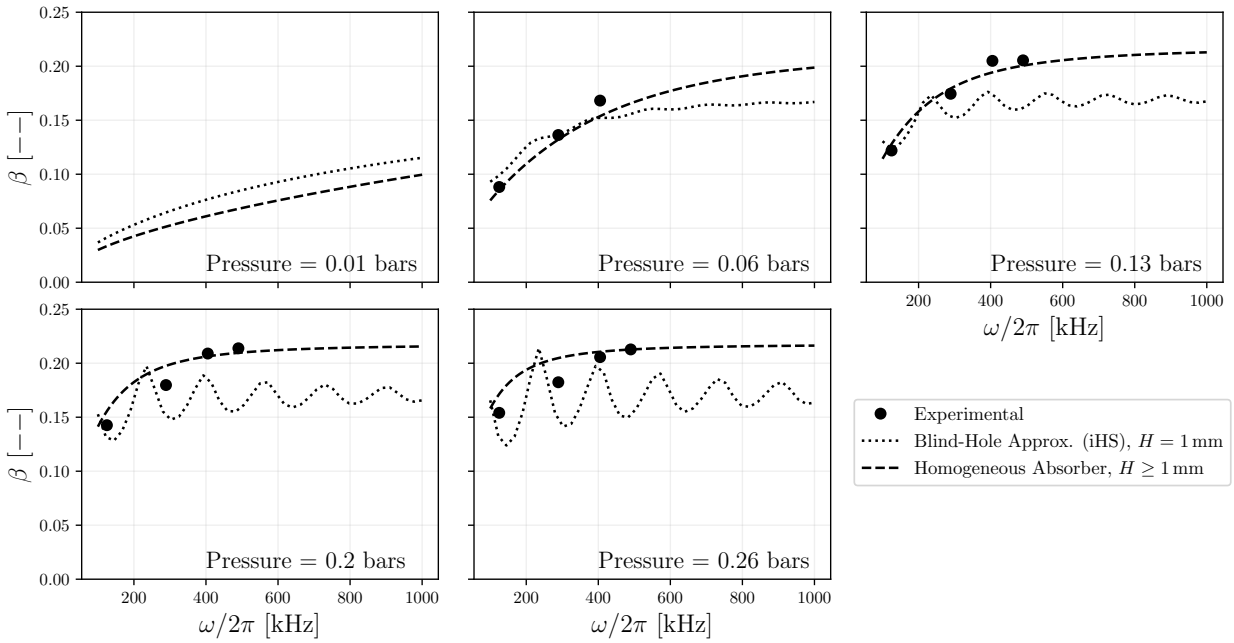

Fig. 14 Comparisons of broadband absorption coefficient behaviors evaluated using experimentally, numerically, and theoretically measured acoustic impedance.

where, κ is the structure factor, Ξ the flow specific resistivity, ϕ the volume porosity, k the wave number, $\omega = 2\pi f$ the angular frequency of incident wave, θ_i the angle of incidence, H the depth of the absorber, and $Z_0 = \rho_0 a_0$ the base impedance measured using ambient temperature T_w. The parameter ω_k is referred to as the breaking frequency of the absorber, and specifies the frequency below which the absorber is expected to perform poorly. A value of $\theta_i = 30^o$ has been assumed for the angle of incidence to emulate the benchtest setup in these calculations. Relevant values for various parameters in equation (2) have been summarized in table 2.

It is worth noting that the acoustic impedance determined this way does not vary much for assumed absorber depths over $H \geq 1$ mm (curves in Figure 14 from the homogeneous absorber theory would be indistinguishable for $H \geq 1$ mm).

For the predictions carried out with a blind-hole porosity assumption, a surface (and hence also volume) porosity of 0.078 is used, as obtained from the processing of the high-resolution C/C surface images. A nominally chosen depth of $H = 1$ mm has been assumed based on visual inspection of depth-wise slices of a C/C sample provided by DLR Stuttgart [25].

Table 2 Parameters used with the absorber theory

Porosity, ϕ	Structure Factor, κ	Resistivity, Ξ	Depth, H or h^*	T_w $[K]$
0.15 [–]	8.0 [–]	13 [MPa s m^{-2}]	5 $\times 10^{-3}$ [m]	295

Figure 13 compares the results obtained experimentally with: (1) an analytical model for volumetric porous absorbers, the Homogeneous Absorber Theory (HAT), and (2) the numerically obtained results with the iHS methodology applied to the blind-hole approximation of the C/C (only considering the 7 cracks in figure 5). It is possible to observe that both absorber theory and the iHS predict similar absorption coefficient trends for low base pressures. These are in good agreement with the lowest base pressure cases explored in the experiments.

As the pressure increases the absorption coefficient predicted based on the blind-hole porosity approximation starts to deviate from both the experimental data and the HAT predictions. We first observe an overall under-prediction of the magnitude of the absorption coefficient, which is attributed to the underestimated volume porosity (by a factor of two) – a natural outcome of the blind-hole approximation. This leads us to conclude that the smaller cracks (ignored in the selection done in figure 5) play an important role in the absorption.

Another important difference observed is the appearance of resonance-like peaks in the absorption predicted by the blind-hole approximation with the iHS formulation, due to the assumed finite depth of the cavities. This behavior is apparent also in the HAT results but only for $H < 1$ mm (not shown). The experimental data is not spaced out finely enough in the frequency domain to be able to address this. A different transducer/receiver would have to be manufactured for different frequencies making it very cumbersome to address this point experimentally. However, especially for higher pressures (above 0.2 bars), the experimental data falls below the HAT predictions for frequencies below 400 kHz. It is not possible to establish with the present data if this is due to a resonant-like, blind-hole porosity variation of the absorption coefficient or just a decreased accuracy of the HAT model for higher pressures. Given the broadband nature of perturbations in hypersonic boundary layers, accounting for the resonant-like behavior of the wall-impedance (were it to be truly present in C/Cs) is expected to be critical towards accurate predictions of the transition dynamics over porous surfaces.

IV. Summary

A joint experimental and numerical effort was undertaken to measure and predict the absorption characteristics of ultrasonically absorptive porous materials with random microstructure under zero-mean-flow conditions. Various measurement techniques were applied such as high speed Schlieren visualization to obtain qualitative information on the acoustic waves. Optical interferometer measurements were conducted to assess the phase shift of the waves due to their interaction with the porous walls. The interferometer measurements were found to be promising. The first tests provided important information on the optical resolution required and the temporal demands on the recording system. Future experiments are planned with a pulsed light source with pulse time in the range of a few nanoseconds to avoid the motion blur and to allow increasing the optical resolution. The transducer based measurements represent the bulk part of the experimental activities. The setup was further refined and now provides reliable information on the absorption coefficient down to 2500 Pa which is of particular interest for applications in the hypersonic flight regime. In the scope of the study the setup was evaluated with respect to the resolvable phase shift. Future measurements will incorporate minor changes to the setup to conduct phase shift measurements. Furthermore, the inverse Helmholtz Solver was used to approximate the complex surface impedance based on a blind-hole model of the C/C only based on the larger cavities extracted from high resolution images of the porous surface. This choice resulted in an underestimated volume porosity by a factor of two with respect to the experimentally determined one via mercury porosimetry. Results were compared to the experiments and to the Homogeneous Absorber Theory. A particularly good agreement was obtained at low pressures, approximately below 0.2 bar, and low frequencies, approximately up to 400 kHz. The discrepancy of the blind-hole approximation is attributed to the underestimated volume porosity, in particular regarding the neglected smaller pores. That indicates the need of a refined model of the surface porosity. Future plans involve impedance predictions in the presence of a shear layer overlying the acoustic absorber with the overall goal to numerically replicate experiments using porous surfaces for transition control.

Acknowledgments

The authors acknowledge the support of the Rosen Center for Advanced Computing (RCAC) at Purdue, the Air Force Office of Scientific Research grants FA9550-18-1-0292 (2018 Young Investigator Program Award), grant FA9550-16-1-0456 and the fruitful discussions with Dr. Ivett Leyva and Prof. Russ Cummings (AFOSR). Victor Sousa also acknowledges the support of the prestigious Lynn Fellowship administered by the interdisciplinary Computational Science and Engineering (CS&E) graduate program at Purdue University. Furthermore, the authors wish to acknowledge the assistance of the technical staff, in particular Jens Steinhoff and Günter von Roden.

References

[1] Malmuth, N., Fedorov, A., Shalaev, V., Cole, J., Khokhlov, A., Hites, M., and Williams, D., "Problems in High Speed Flow Prediction Relevant to Control," *2nd AIAA, Theoretical Fluid Mechanics Meeting*, 1998. doi:10.2514/6.1998-2695, aIAA 98-2695.

[2] Fedorov, A. V., Malmuth, N. D., Rasheed, A., and Hornung, H. G., "Stabilization of Hypersonic Boundary Layers by Porous Coatings," *AIAA*, Vol. 39, No. 4, 2001, pp. 605–610.

[3] Rasheed, A., Hornung, H. G., Fedorov, A. V., and Malmuth, N. D., "Experiments on Passive Hypervelocity Boundary-Layer Control Using an Ultrasonically Absorptive Surface," *AIAA*, Vol. 40, No. 3, 2002, pp. 481–489.

[4] Fedorov, A. V., Kozlov, V., Shiplyuk, A., Maslov, A., and Malmuth, N., "Stability of Hypersonic Boundary Layer on Porous Wall with Regular Microstructure," *AIAA Journal*, Vol. 44, No. 8, 2006, pp. 1866–1871.

[5] Fedorov, A. V., Shiplyuk, A., Maslov, A., Burov, E., and Malmuth, N., "Stabilization of a hypersonic boundary layer using an ultrasonically absorptive coating," *Journal of Fluid Mechanics*, Vol. 479, 2003, pp. 99–124. doi:10.1017/S0022112002003440.

[6] Maslov, A. A., Shiplyuk, A., Sidorenko, A., Polivanov, P., Fedorov, A., Kozlov, V., and Malmuth, N., "Hypersonic Laminar Flow Control Using a Porous Coating of Random Microstructure," *44th AIAA Aerospace Sciences Meeting and Exhibit*, Reno, Nevada, 2006. AIAA 2006-1112.

[7] Maslov, A. A., Fedorov, A. V., Bountin, D. A., Shiplyuk, A. N., Sidorenko, A. A., Malmuth, N., and Knauss, H., "Experimental study of transition in hypersonic boundary layer on ultrasonically absorptive coating with random porosity," *46th AIAA Aerospace Sciences Meeting and Exhibit*, Reno, Nevada, 2008. AIAA 2008-587.

[8] Lukashevich, S. V., Morozov, S. O., and Shiplyuk, A. N., "Experimental study of the effect of a passive porous coating on disturbances in a hypersonic boundary layer 1. Effect of the porous coating length," *Journal of Applied Mechanics and Technical Physics*, Vol. 54, No. 4, 2013, pp. 572–577. doi:10.1134/S002189441304007X.

[9] Wagner, A., Hannemann, K., Wartemann, V., and Giese, T., "Hypersonic boundary-layer stabilization by means of ultrasonically absorptive carbon-carbon material - Part 1: Experimental Results," *51st AIAA Aerospace Sciences Meeting*, Texas, 2013. doi:10.2514/6.2013-270, URL `http://dx.doi.org/10.2514/6.2013-270`, aIAA 2013-0270.

[10] Turner, J., Hörschgen, M., Jung, W., Stamminger, A., and Turner, P., "SHEFEX Hypersonic Re-entry Flight Experiment; Vehicle and Subsystem Design, Flight Performance and Prospects," *14th AIAA/AHI Space Planes and Hypersonic Systems and Technologies Conference*, 2006. AIAA 2006-8115.

[11] Weihs, H., Longo, J., and Turner, J., "Key Experiments within the SHEFEX II Mission," *IAC 2008*, Glasgow, Scottland UK, 2008.

[12] Wagner, A., Wartemann, V., Hannemann, K., Kuhn, M., and Dittert, C., "The Potential of Ultrasonically Absorptive TPS Materials for Hypersonic Vehicles," *20th AIAA International Space Planes and Hypersonic Systems and Technologies Conference*, 2015.

[13] Wagner, A., Hannemann, K., and Kuhn, M., "Ultrasonic absorption characteristics of porous carbon-carbon ceramics with random microstructure for passive hypersonic boundary layer transition control," *Experiments in Fluids*, Vol. 55, No. 6, 2014, 1750. doi:10.1007/s00348-014-1750-4.

[14] Patel, D., Gupta, P., Scalo, C., Rothermel, T., and Kuhn, M., "Towards Impedance Characterization of Carbon-Carbon Ultrasonically Absorptive Coatings via the Inverse Helmholtz Problem," *55th AIAA Aerospace Sciences Meeting*, 2017, p. 0460. doi:10.2514/6.2017-0460, URL `http://dx.doi.org/10.2514/6.2017-0460`, aIAA-2017-0460.

[15] Patel, D., Gupta, P., and Scalo, C., "Impedance Calculation via the Inverse Helmholtz Solver (iHS)," *arXiv preprint arXiv:1708.02069*, 2017.

[16] Müller, G., and Möser, M., *Handbook of engineering acoustics*, Springer Science & Business Media, 2012.

[17] Fedorov, A. V., Kozlov, V. F., and Addison, R. C., "Reflection of acoustic disturbances from a porous coating of regular microstructure," *5th AIAA Theoretical Fluid Mechanics Conference*, 2008. AIAA 2008-3902.

[18] Brès, G. A., Colonius, T., and Fedorov, A. V., "Acoustic Properties of Porous Coatings for Hypersonic Boundary-Layer Control," *AIAA Journal*, Vol. 48, No. 2, 2010, pp. 267–274. doi:10.2514/1.40811.

[19] Kreis, T., *Holographic interferometry*, Akademie Verlag, Berlin, 1996.

[20] Roddier, C., and Roddier, F., "Interferogram analysis using Fourier transform techniques." *Applied optics*, Vol. 26, 1987, pp. 1668–73.

[21] Nakadate, S., and Saito, H., "Fringe scanning speckle-pattern interferometry," *Appl. Opt.*, Vol. 24, No. 14, 1985, pp. 2172–2180. doi:10.1364/AO.24.002172, URL `http://ao.osa.org/abstract.cfm?URI=ao-24-14-2172`.

[22] Vest, C. M., *Holographic interferometry*, Wiley, New York, 1979.

[23] Kujawinska, M., "Spatial phase measurement methods," *Interferogram Analysis*, 1993. URL `https://ci.nii.ac.jp/naid/10016235849/en/`.

[24] Wagner, A., Kuhn, M., Martinez Schramm, J., and Hannemann, K., "Experiments on passive hypersonic boundary layer control using ultrasonically absorptive carbon-carbon material with random microstructure," *Experiments in Fluids*, Vol. 54, No. 10, 2013. doi:10.1007/s00348-013-1606-3.

[25] Patel, D., "Impedance Characterization of Carbon-Carbon Ultrasonically Absorptive Coatings Via the Inverse Helmholtz Solver," , 2017.